J Mater Sci (2011) 46:4953–4963
DOI 10.1007/s10853-011-5412-0

Precipitate alterations in the heat-affected zone of a Grade 100 microalloyed steel

Kioumars Poorhaydari · Douglas G. Ivey

Received: 1 September 2010 / Accepted: 18 February 2011 / Published online: 9 March 2011

Abstract Microalloy precipitate alterations (particularly dissolution) in the heat-affected zone (HAZ) of a Grade 100 steel, microalloyed by titanium, niobium, and vanadium and produced in the form of a plate with a thickness of 8 mm, was examined both theoretically and experimentally. For theoretical analysis of precipitate dissolution, pairs of effective peak temperature and holding time were extracted from the thermal cycles of welding, and were superimposed on the Ashby and Easterling non-equilibrium solubility curves for different fractions of precipitate dissolution. Intersections between the effective *T–t* curves and the non-equilibrium solubility curves gave *critical* pairs of effective peak temperature and holding time for dissolution of different fractions of a precipitate, which resulted in the establishment of *precipitate dissolution profiles* in the HAZ. Experimental analysis of precipitate alterations was carried out using carbon extraction replicas in a transmission electron microscope. The theoretical analyses were in agreement with experimental results, showing that it is the dissolution of small Nb-rich particles that paves the way to grain growth in the coarse-grained HAZ. Reprecipitation was generally suppressed in the low heat-input weld sample. There was some reprecipitation in the higher heat-input weld samples. Coarsening of TiN did not occur in the HAZ, due to the large size of these particles in the steel examined.

K. Poorhaydari (✉) · D. G. Ivey
Department of Chemical and Materials Engineering,
University of Alberta, Edmonton, AB T6G 2V4, Canada
e-mail: kioumars@ualberta.ca

Introduction

High-strength, low-carbon microalloyed steels are a group of high-strength low-alloy (HSLA) steels produced in the as-rolled condition. Thermomechanical controlled processing (TMCP), consisting of controlled rolling and interrupted/accelerated cooling, is employed for the control of austenite recrystallization and grain growth, as well as the austenite-to-ferrite phase transformation [1–3]. Precipitation is achieved by the addition of a small amount of microalloying elements such as titanium, niobium, and vanadium (usually 0.01–0.1 wt% each and <0.2 wt% combined). All these processing factors have led to an increase in strength, which can be attributed primarily to grain refinement, as well as to precipitation hardening to some extent [4, 5].

The weld thermal cycle causes alterations in the precipitate composition, size distribution, and volume fraction through dissolution, coarsening, and reprecipitation. These alterations affect the mechanical properties of the heat-affected zone (HAZ) directly, through a change in precipitate distribution and precipitation hardening, or indirectly, by affecting the austenite grain growth and effective composition of the austenite (changed by dissolution of precipitates). It is, therefore, necessary to understand the changes within different sub-regions of the HAZ for different heat inputs in new grades of high-strength microalloyed steel.

The objective of this article is to evaluate precipitate alterations (particularly precipitate dissolution) in the HAZ of microalloyed steels through kinetic calculations as well as experimental observations. Since most of the precipitates that change during the weld thermal cycle were submicron in size, high-resolution transmission electron microscopy (TEM) was used to resolve them. Carbon extraction replicas were used as TEM samples in this study.

In this study we are focusing on a type/grade of microalloyed steel (i.e., Grade 100), whose microstructure was examined elsewhere [5, 6]. The microstructure was made up of primarily quasi-polygonal ferrite and bainitic ferrite, with smaller amounts of M/A constituents. Microalloy precipitates appeared in different sizes, shapes, and compositions. Large cuboidal TiN particles (2–8 μm) were formed in the liquid, during solidification or during reheating. Intermediate-size Ti-rich and Nb-rich carbonitrides (50–300 nm) were formed mostly during cooling of the austenite after reheating. They had different shapes including elliptical, cuboidal, and sliver-like configurations. Small Nb/Mo carbides (<20 nm, with an average diameter of 4.3 ± 2.4 nm), with considerable amounts of Ti and V were formed either during rolling of the austenite below the no-recrystallization temperature (i.e., strain-induced precipitation) or in ferrite at the stop cooling temperature following accelerated cooling (i.e., general precipitation). No interphase precipitation was noted, which was due to accelerated cooling at moderate cooling rates (∼15–20 °C/s), which is believed to largely suppress interphase precipitation [7].

Theoretical analysis

Particle dissolution

As the temperature rises due to the weld thermal cycle, the precipitates may start to dissolve to some degree, since the solubility of the microalloy elements increases with increasing temperature. Two sets of information are needed to evaluate how much a precipitate is dissolved due to a thermal cycle at a certain location in the weld HAZ and for a given heat input: first, non-equilibrium solubility information for that precipitate, and second, the thermal cycle characteristics (effective peak temperature and dwell time) at that location and for that weld sample.

Non-equilibrium solubility curves

The theory of particle dissolution, as a result of superheating above the equilibrium temperature of particle dissolution, T_s, and applied to the rapid thermal cycle of welding, has been developed by Ashby and Easterling [8, 9]. The particles were assumed to be spherical. The two resulting equations from their analysis that relates the time of dissolution, t, to the temperature of superheating, T, are as follows:

$$f = \frac{1}{1 + \left[\frac{t^*}{t}\exp -\frac{Q_V}{R}\left(\frac{1}{T^*} - \frac{1}{T}\right)\right]^{3/2}} \quad (1)$$

$$T_S = \frac{B}{A - log\left[\frac{C_M^a C_X^b}{f^{a+b}}\right]} \quad (2)$$

f is the volume fraction to be dissolved, Q_V is the activation energy for diffusion of the metal atom, t^* is the time at which dissolution is complete at a temperature T^*, C is the concentration of elements M (metal atom) or X (carbon or nitrogen) in the reaction '$aM + bX \leftrightarrow M_aX_b$', R is the gas constant, and A and B are constants of the solubility product k_S. A pair of values for t^* and T^* were used from a set of experiments by Ikawa et al. (as cited by Easterling [10]), where the time for dissolution of NbC at the equilibrium temperature of dissolution (1077 °C) was estimated to be about 20 s. Combining the above two equations will give Eq. 3. Values for Q_V were the approximated values used by Easterling (Table 1).

$$t = \frac{t^* \exp\left[\frac{-Q_V}{R}\left(\frac{1}{T^*} - \frac{1}{T_S}\right)\right]}{\left[\left(\frac{\exp 2.3[A - B/T_S]}{k_S}\right)^{1/(a+b)} - 1\right]^{2/3}} \quad (3)$$

To find the non-equilibrium solubility curves for different fractions of precipitate dissolution, the solubility product k_S in Eq. 3 was replaced with the value from Eq. 4 for a given fraction of precipitate solution, f. In Eq. 4, M_{MX} is the wt% M present as MX, X_{MX} is the wt% of X present as MX, [M] is the wt% of M dissolved in the matrix and [X] is the wt% of X dissolved in the matrix. This modification is believed to make solubility product estimations more accurate than the method used by Ashby and Easterling [8], as it also takes into account the amount of solutes already in the matrix. The amount already in the matrix is the sum of the residual levels in solid solution in the base metal (BM) and the solutes added to the matrix due to the dissolution of precipitates with higher solubility [11]. The non-equilibrium solubility curves for several fractions of dissolution of NbC in the Grade 100 steel are shown in Fig. 1.

$$k_S = (f \cdot M_{MX} + [M])(f \cdot X_{MX} + [X]) \quad (4)$$

Effective temperature and time for a weld thermal cycle

The non-equilibrium solubility curves were originally constructed based on isothermal heating above the equilibrium

Table 1 Approximate values of activation energy for diffusion of various metal atoms in iron [10]

Metal element	Ti	Nb	V	Mo
Q_V/RT_m	14.4	23.1	16.1	20.1

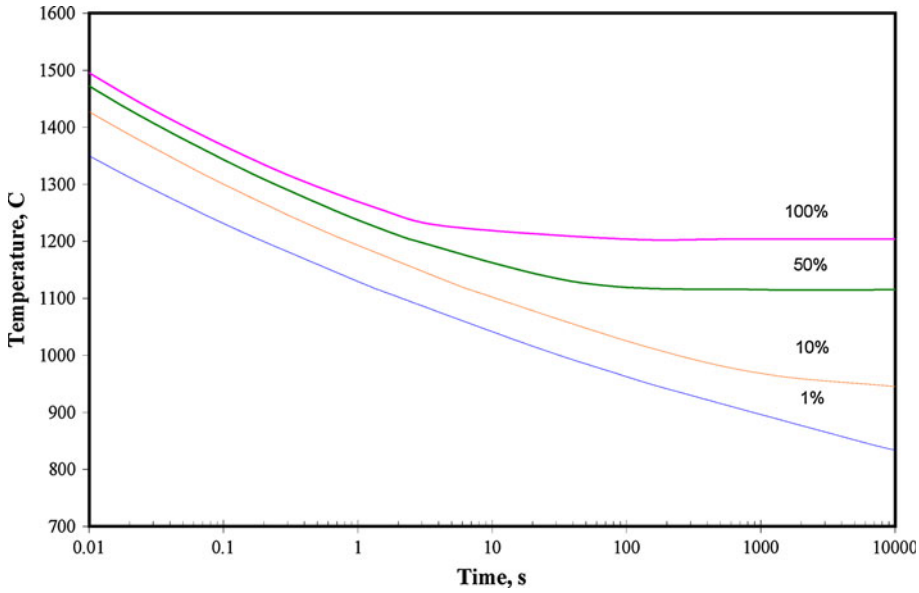

Fig. 1 Non-equilibrium solubility curves for several fractions of precipitate dissolution for NbC in the Grade 100 steel

temperature. It was assumed here that the portion of the weld thermal cycle with its temperature above the equilibrium dissolution temperature of a precipitate is responsible for dissolution (Fig. 2). The larger this portion, the more efficient will be the diffusion which controls the rate of dissolution. An effective peak temperature, $T_{\text{P-Eff}}$, can be calculated over an effective time, t_{Eff}, so that the diffusion criterion (or kinetic strength of the thermal cycle) under isothermal heating would be equal to that of the actual thermal cycle. The diffusion criterion used here is defined as the product $D{\cdot}t$, which is a function of diffusion distance:

$$D \cdot t = D_0 \cdot t \cdot \exp\left(\frac{-Q}{RT}\right) \tag{5}$$

Therefore,

$$\exp\left[\frac{-Q}{RT_{\text{P-Eff}}}\right] t_{\text{Eff}} = \int_{t_S}^{t_S+t_{\text{Eff}}} \exp\left[\frac{-Q}{RT(t)}\right] \mathrm{d}t = I \tag{6}$$

D_0 is the frequency factor, D is the diffusion constant, $T(t)$ is temperature at time t during the weld thermal cycle, Q is the activation energy for diffusion of metal atom M in iron, t_S is the moment during the weld thermal cycle when the temperature goes above the equilibrium temperature for dissolution of the precipitate (T_S), and I is the integral of the curve $\frac{-Q}{RT(t)}$ vs. t over the time t_{Eff}. Equation 6 can be rewritten as the following equation that was used to calculate the effective peak temperature:

$$T_{\text{P-Eff}} = \frac{-Q}{R\ln(I/t_{\text{Eff}})} \tag{7}$$

The effective time, t_{Eff}, is in fact the dwell time above T_S. As seen in Fig. 2, the effective peak temperature ($T_{\text{P-Eff}}$) is considerably higher than the average temperature between T_P and T_S (as denoted by $T_{\text{P-Average}}$). This is because diffusion is exponentially faster at high temperatures. From these calculations, a pair of $T_{\text{P-Eff}}$ and t_{Eff} can be obtained for a thermal cycle and a given dissolution temperature. Estimated temperature–time (T–t) curves were used for each weld sample and for several dissolution temperatures representing different fractions of dissolution [11]. From the calculations for various values of T_P and various fractions of dissolution, a graph like the one shown in Fig. 3 was obtained. The graph shows how much time (t_{Eff}) is available at an isothermal effective peak temperature ($T_{\text{P-Eff}}$) for dissolution of different fractions of a precipitate (i.e., NbC in this particular graph).

Superimposing the available $T_{\text{P-Eff}}$ and t_{Eff} data on the non-equilibrium solubility curves will show if the portion of the thermal cycles above the dissolution temperature is large enough to cause dissolution (Fig. 4), i.e., if the pairs of effective time and temperature lie above the solubility curves. Moreover, the Intersections between the effective T–t curves and the non-equilibrium solubility curves will determine *critical* pairs of $T_{\text{P-Eff}}$ and t_{Eff} for dissolution of a fraction f of a precipitate. These pairs are denoted with circles in Fig. 4. Then, finding that there is a linear relationship between the T_P and $T_{\text{P-Eff}}$ [11], the corresponding critical T_P for the critical $T_{\text{P-Eff}}$ can be interpolated or extrapolated. This critical T_P can be related to a distance from the fusion line through the peak temperature profiles [12]. The same procedure was applied for 1, 5 and 10% dissolution of TiN (TiN dissolution in the HAZ is very limited).

The findings from the above analyses are summarized in Fig. 5 as *precipitate dissolution profiles*, which show the fraction of precipitate dissolution vs. normalized distance

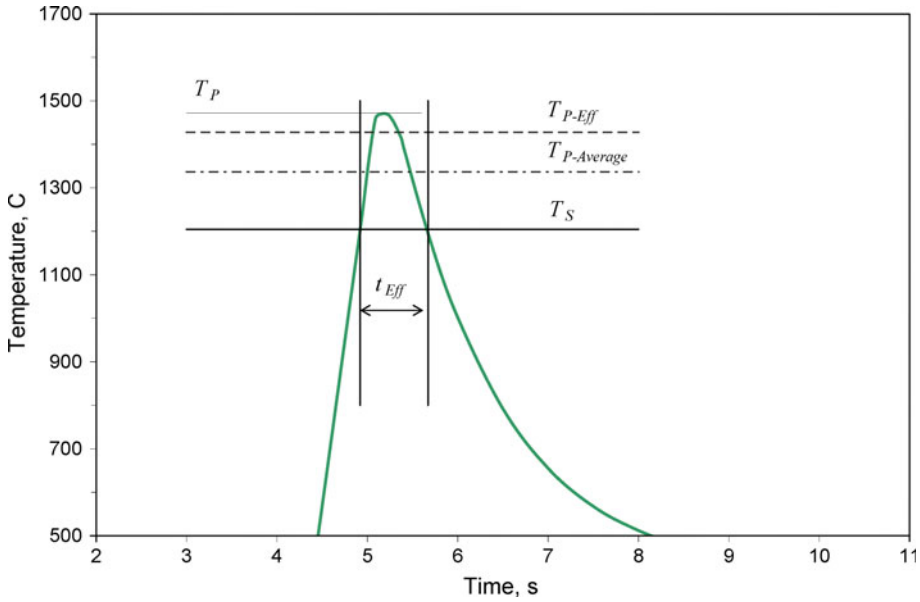

Fig. 2 Effective peak temperature and time for complete dissolution of NbC at $T_P = 1468$ °C

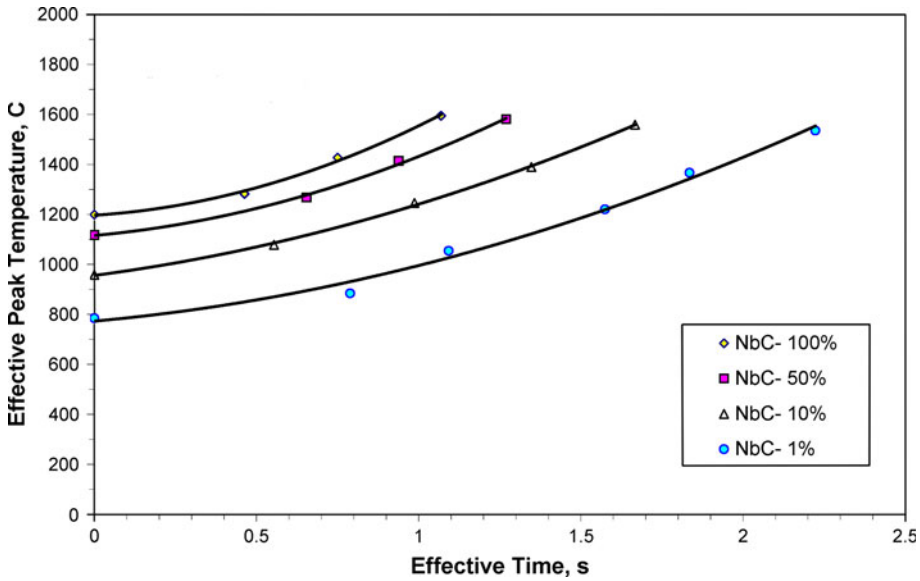

Fig. 3 Effective peak temperature and effective time available for dissolution of NbC at several locations (or several T_P) and for various fractions of dissolution shown for a heat input of 0.5 kJ/mm

(with respect to the HAZ width) from the fusion line for several heat inputs. Also, the approximate locations of sub-region boundaries and their corresponding peak temperature values (averaged for the three weld samples) are superimposed on the graphs. The graph shows that dissolution of NbC does not occur in the inter-critical HAZ (ICHAZ) or in most of the fine-grained HAZ (FGHAZ). Dissolution of NbC starts close to the boundary between the FGHAZ and coarse-grained HAZ (CGHAZ) and is completed (100% dissolution) somewhere in the CGHAZ, the exact locations depending on the heat input. TiN dissolution starts in the CGHAZ but barely exceeds 10–15% before the fusion line.

In addition, the solute levels in the matrix as a result of precipitate dissolution can be calculated, as shown in Fig. 6a and b for two values of heat input for the Grade 100 steel. The results show the effective austenite composition in the various HAZ sub-regions, which affects the hardenability. Note that very little reprecipitation occurs in austenite during the cooling leg of the weld thermal cycle (most of small particle reprecipitation in the CGHAZ occurs after austenite transformation) and therefore the values obtained should represent the austenite composition prior to transformation.

Particle coarsening

Particle coarsening results from the growth of large particles at the expense of smaller particles (Ostwald ripening). It occurs with the average precipitate size increasing, while maintaining a virtually constant volume fraction. The

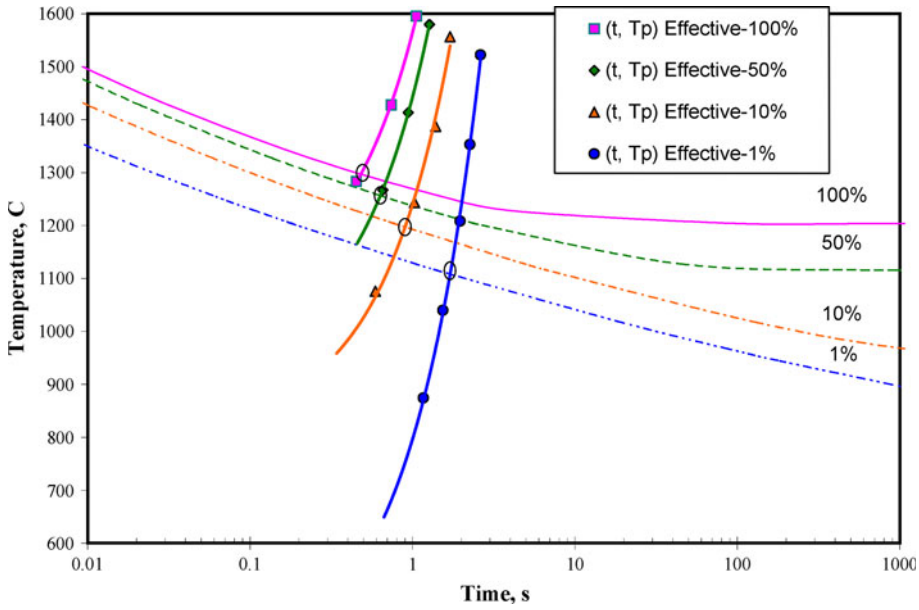

Fig. 4 Superposition of the effective temperature-effective time curves on the non-equilibrium solubility curves for NbC in the Grade 100 steel with a heat input of 0.5 kJ/mm

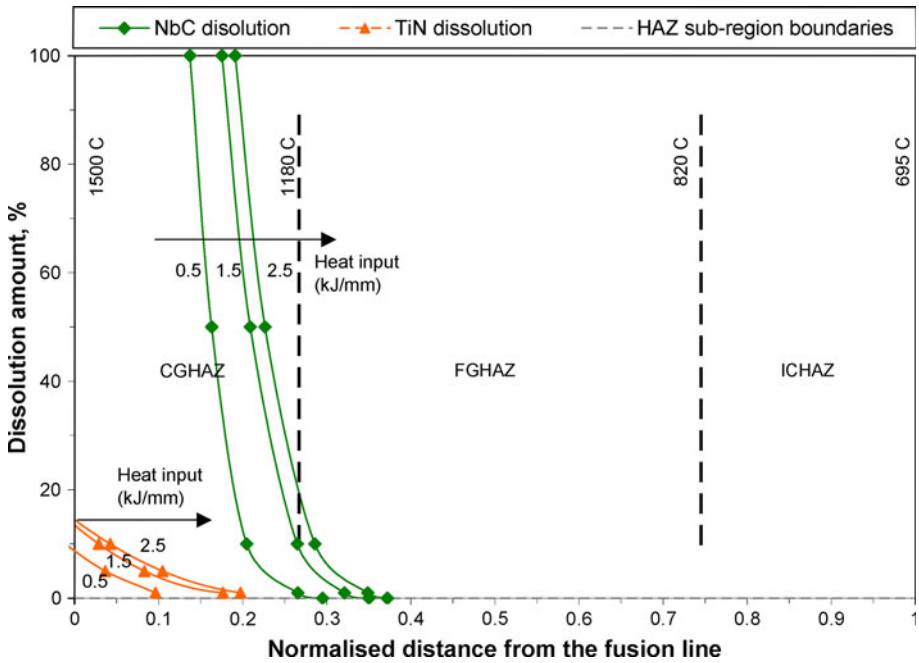

Fig. 5 Precipitate dissolution profiles across the HAZ in the Grade 100 steel for heat inputs of 0.5, 1.5, and 2.5 kJ/mm

driving force for precipitate coarsening is the reduction in the interfacial area. Equation 8 shows a relationship based on the Lifshitz–Wagner theory for Ostwald ripening, that approximates the change in the particle size, given the temperature, $T(t)$, and the activation energy for diffusion of metal atoms between particles, Q_V [10].

$$r^3 - r_0^3 = \int_0^\infty \frac{A_C}{T(t)} \exp - \left(\frac{Q_V}{RT(t)} \right) dt = I \tag{8}$$

r and r_0 are the new and original particle radii, respectively, and A_C is a constant depending on the matrix composition. Unfortunately, there are no measured values for the coarsening of precipitates in the Grade 100 steel that can be used to determine the constant A_C in the equation, but with some approximations the experimental values of Easterling [10] for coarsening of very small TiN particles can be used. The calculation for A_C yielded values of approximately 7.20×10^{-16} and 2.00×10^{-15} K s^{-1} m^3, for thick- and thin-plate conditions, respectively [11].

Table 2 shows the amount of coarsening for various sizes of TiN particles after applying the values of A_C to a thermal cycle at a location close to the fusion line ($T_P = 1435$ °C) and a high heat input of 2.5 kJ/mm, where

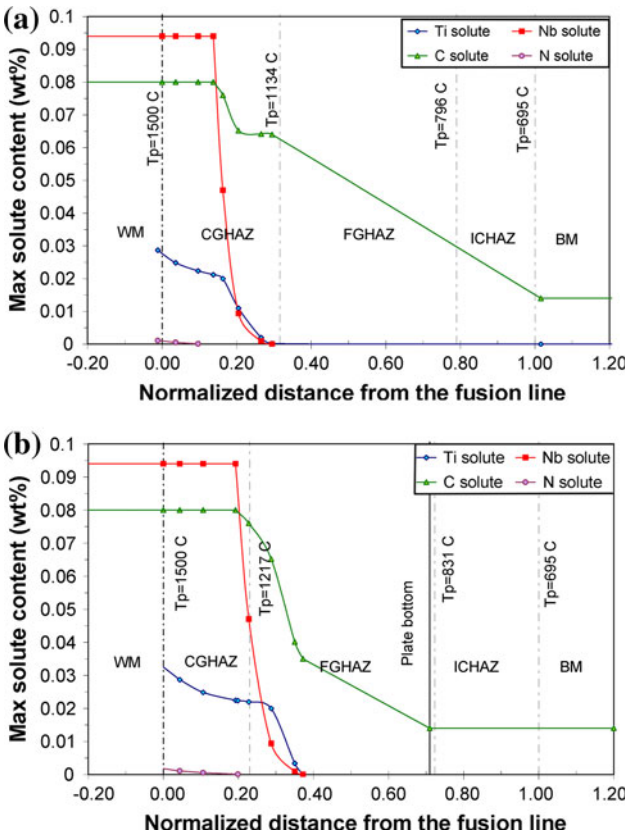

Fig. 6 Maximum solute level in the matrix across the HAZ of the Grade 100 steel for heat inputs of: **a** 0.5 kJ/mm; **b** 2.5 kJ/mm

the coarsening of TiN particles is expected to be the most pronounced. The calculations were made for two heat transfer conditions, namely thick plate and thin plate. As can be seen, coarsening is considerable only when the initial particle size is very small (i.e., a few nanometers). For TiN particles in Grade 100 steel, namely intermediate-size precipitates (~200 nm on average) and large precipitates (~4 μm on average), coarsening can be neglected. The reason that coarsening of larger particles does not occur over typical weld thermal cycles, is that diffusion distance between particles is too large and the surface to volume ratio is too small.

Particle reprecipitation

As the weld sample cools down below the equilibrium dissolution temperature of a precipitate during the cooling leg of a weld thermal cycle, the solubility limits for the microalloying elements drop. The result is a tendency for reprecipitation of the particles that dissolved at temperatures above the dissolution temperature of the particle, provided that the cooling rate is low enough to allow diffusion of microalloying atoms. In most cases, however, cooling rates during welding are too high, leaving the matrix relatively supersaturated with microalloying elements.

Table 2 Estimation of coarsening of TiN particles based on the initial particle size

r_0, nm		4	40	100	2000
r, nm	Thick plate	7.4	40.1	100.0	2000
	Thin plate	10.1	40.2	100.0	2000
$(r - r_0)/r_0$	Thick plate	0.86	1.81×10^{-3}	1.16×10^{-4}	1.45×10^{-8}
	Thin plate	1.52	4.99×10^{-3}	3.21×10^{-4}	4.01×10^{-8}

The intention of this article is not to get into the kinetic analysis of precipitate reprecipitation during welding. Some of the results of isothermal precipitation experiments, however, are discussed here as they can give insight to whether or not such analysis is relevant. It has been reported that the precipitation of Nb-rich carbonitrides at 900 °C, even after 67% reduction (which is a very high amount of deformation), can take up to a minute. With smaller amounts of deformation, practiced in commercial rolling passes, the precipitation time could take several minutes or even several tens of minutes [4]. For a weld thermal cycle, holding at specific temperatures does not occur and there is no external deformation to accelerate precipitation (assuming that the effect of weld thermal stresses on reprecipitation would be much less than the effect of mechanical deformation during rolling that generates slip bands). Therefore, it seems reasonable that reprecipitation is largely suppressed. If precipitation happens, it should occur in high heat-input weld samples, at relatively low temperatures (likely in ferrite) and in the form of small particles in the matrix, on the grain/sub-grain boundaries or on intermediate-size particles. Suppression of reprecipitation will result in some solute supersaturation in the HAZ, which not only increases the hardenability, but also increases the matrix strength/hardness.

Experimental procedure

The Grade 100 microalloyed steel used in this study was a low-carbon steel, microalloyed with Ti, Nb, and V and produced in the as-rolled condition. The designation 100 refers to the specified minimum yield strength (SMYS) in 'ksi' (approximately 690 MPa). The chemical composition of the steel is shown in Table 3. The P_{cm} value (i.e., the composition parameter for low-carbon microalloyed steels according to the Ito–Bessyo equation) is also included. The as-received material was in the form of a plate with a thickness of 8 mm.

HAZ samples were obtained by applying single-pass autogenous gas tungsten arc welding (GTAW with no filler metal) on the horizontal plates. Nominal heat inputs of

Table 3 Chemical composition of the Grade 100 microalloyed steel (wt%)

C	Mn	Ti	Nb	V	Mo	N	Others	P_{cm}
0.08	1.80	0.06	0.09	0.05	0.30	0.01	<1.2	0.24

$P_{cm} = \%C + \frac{\%Mn+\%Cr+\%Cu}{20} + \frac{\%Si}{30} + \frac{\%Mo}{15} + \frac{\%V}{10} + \frac{\%Ni}{60} + 5\%B$

0.5–2.5 kJ/mm were applied by selecting an arc voltage of 12.5 V, an arc current of 150 A and travel speeds of 0.7–4.0 mm/s. Thermocouples were embedded in the plates to record the weld thermal cycle at different locations (i.e., distances from the fusion line). A full description of the welding and thermal analysis is given elsewhere [12].

Metallographic samples were prepared from both transverse and longitudinal sections (w.r.t. welding direction). The polished samples were etched with 2% Nital. A conventional carbon extraction replica method [13] was used to prepare TEM samples from four distinct regions, namely the BM, ICHAZ, FGHAZ, and CGHAZ. Relatively site-specific carbon replicas were prepared by masking off regions of interest on the metallographically prepared samples from the longitudinal weld sections, wherever possible. A 5% Nital solution was used for separation of the replicas from the substrate. Replicas were examined in a JEOL 2010 TEM operated at 200 kV and equipped with an ultra-thin-window energy dispersive X-ray (EDX) system. In order to obtain the size distribution of the small precipitates, ten bright-field TEM images taken at a magnification of 100,000× from different fields of view were examined individually. The precipitates in each micrograph were measured individually using the 'callipers' tool in ImagePro® software.

TEM results

TEM replicas from BM, ICHAZ, FGHAZ, and CGHAZ were examined for three heat inputs (0.5, 1.5, and 2.5 kJ/mm). The BM examination results have been presented elsewhere in detail [5, 14]. Since no significant change in precipitates was noted in the ICHAZ (in agreement with theoretical analysis results), only the results from the FGHAZ and CGHAZ are presented here.

Large TiN precipitates were not examined here as they do not change much during the typical weld thermal cycles in the HAZ due to their stability. Large TiN precipitates are too large to be captured by replicas and can be observed in a scanning electron microscope or an optical microscope. Characterization of the precipitates with the aid of selected area diffraction (SAD) and energy dispersive X-ray (EDX) analysis has been carried out fully in the BM and partly in the HAZ [11], so those results are not presented here. The main focus of this section is to show the dissolution and reprecipitation behavior of the precipitates as a function of peak temperature and heat input in the FGHAZ and CGHAZ.

FGHAZ

Figure 7 shows a series of bright-field TEM images from the FGHAZ of different weld samples (i.e., different heat inputs). The top row depicts the intermediate-size particles, which were mostly complex compounds of Ti/Nb carbonitrides, some rich in Ti and some rich in Nb. Examination of these precipitates in several fields of view revealed more or less the same type and size distribution among the different weld samples, indicative of little or no precipitate dissolution in the FGHAZ, consistent with theoretical analysis results.

The bottom row in Fig. 7 shows micrographs taken at a higher magnification, depicting small microalloy carbides. These carbides were rich in Nb and Mo with some Ti and V. Table 4 shows the result of size measurements, as obtained from the replicas. The size distribution curves are shown in Fig. 8, including the size distribution curve for the small precipitates in the BM for comparison. As apparent from the curves in Fig. 8 and the average sizes (i.e., arithmetic mean) in Table 4, very little variation in size distribution and average size occurred for small precipitates. This observation suggests that even the small precipitates had likely not dissolved in the FGHAZ for the heat inputs applied (which is in support of theoretical analysis results). Had the small precipitates dissolved and reprecipitated in the FGHAZ sub-region, they would most likely have a different size distribution and average size. The small particles would also show a preference for reprecipitation at the grain boundaries, which was not observed.

CGHAZ

Figure 9 shows a series of bright-field TEM images from the CGHAZ of different weld samples. Again, the top row depicts the intermediate-size particles and the bottom row depicts the small microalloy carbides. Examination of the intermediate-size precipitates in several fields of view revealed that the Nb-rich particles were dissolved to a large extent in the CGHAZ, so that no Nb-rich particles were found in the CGHAZ of 2.5 kJ/mm weld sample. The above observations are consistent with the theoretical analysis that suggested NbC dissolution starts close to the boundary between the FGHAZ and the CGHAZ and ends in the CGHAZ not too far from the boundary with the FGHAZ (the distance depends on the heat input). The higher heat-input weld samples had larger fractions of

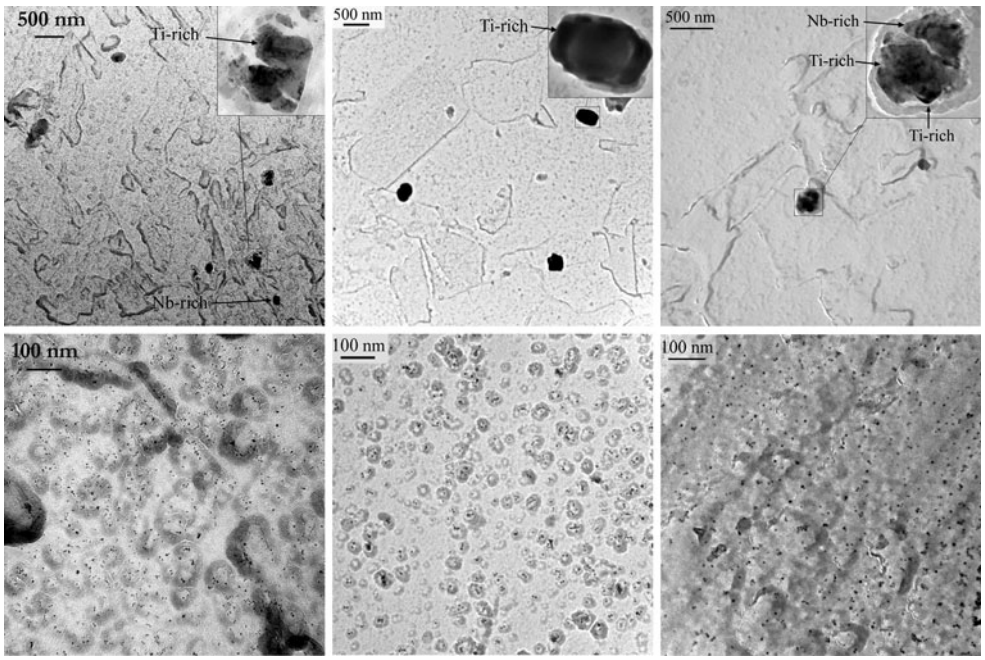

Fig. 7 Bright-field TEM images of intermediate-size precipitates (*top*) and small precipitates (*bottom*) for several heat inputs (i.e., 0.5, 1.5 and 2.5 kJ/mm, from left to right) in the FGHAZ

Table 4 Fine-precipitate size measurements in BM and FGHAZ (several heat inputs) of the Grade 100 steel

Region	*n*	Area covered (μm^2)	Min (nm)	Max (nm)	Average (nm)	S.D. (nm)
BM	490	2.54	0.9	16.4	4.6	2.4
FGHAZ-0.5	1141	2.54	0.9	13.6	4.2	1.7
FGHAZ-1.5	644	1.69	0.9	13.6	4.2	1.7
FGHAZ-2.5	850	2.54	0.9	20.4	4.5	2.4

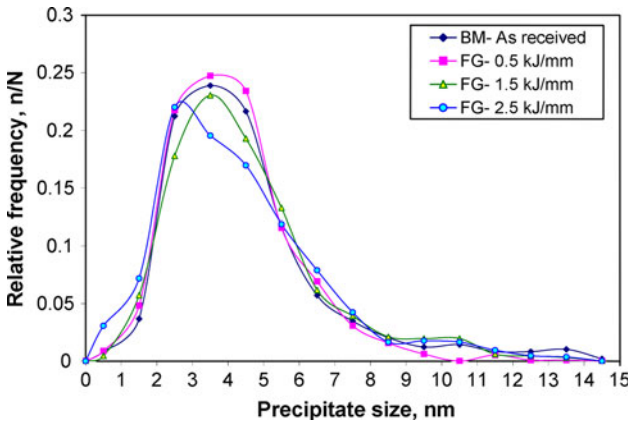

Fig. 8 Comparison of small-precipitate size distribution in the BM and FGHAZ (several heat inputs)

dissolution at a given peak temperature (or normalized distance from the fusion line) than the low heat-input weld sample. Ti-rich carbonitrides were less affected and still present on the replicas, which is also consistent with theoretical analysis results.

Examination of the replicas at a higher magnification revealed that the CGHAZ of the 0.5 kJ/mm weld sample was devoid of small precipitates. The small precipitates in the CGHAZ of the higher heat-input weld samples were much coarser than those in the BM and the FGHAZ and showed agglomeration and higher densities at the grain and lath boundaries of the martensitic (0.5 kJ/mm) or bainitic (1.5 and 2.5 kJ/mm) structures of the matrix. Small precipitates were also observed on the remaining intermediate-size Ti-rich particles. The above observations indicate that the small precipitates, which were rich in Nb and Mo, had dissolved completely in the CGHAZ. Reprecipitation was generally suppressed in the low heat-input weld sample, due to the high cooling rate and the relatively low transformation temperatures for austenite. Reprecipitation occurred in the CGHAZ of the higher heat-input weld samples (having lower cooling rates and higher transformation temperatures). The complete dissolution of small precipitates (as compared with the intermediate-size particles) was partially due to their small sizes (larger surface to volume ratios which facilitate dissolution) and partially due to having more V and Mo

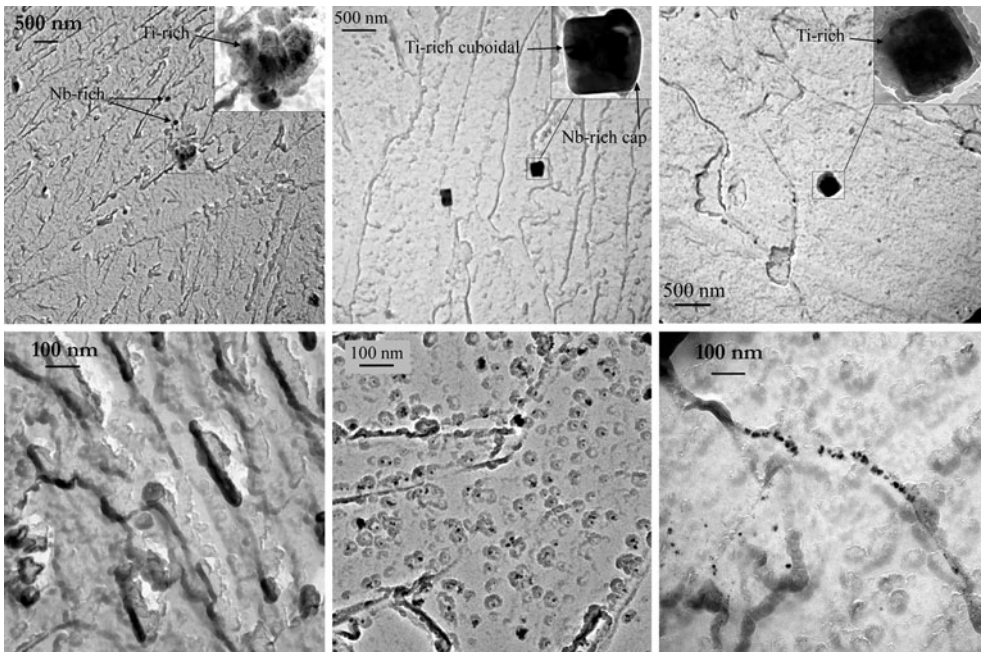

Fig. 9 Bright-field TEM images of intermediate-size precipitates (*top*) and small precipitates (*bottom*) for several heat inputs (i.e., 0.5, 1.5 and 2.5 kJ/mm, from left to right) in the CGHAZ

dissolved in them (not taken into consideration in theoretical analysis).

Discussion

The results for the theoretical analysis of precipitate dissolution across the HAZ of the Grade 100 microalloyed steel for several weld samples (heat inputs of 0.5, 1.5, and 2.5 kJ/mm) are generally in agreement with the experimental results. It was demonstrated that Ashby–Easterling theory of particle dissolution can be used to establish precipitate dissolution profiles across the HAZ of a microalloyed steel, when pairs of effective peak temperature and holding time are calculated from the thermal cycles (actual or predicted [12]) at several locations across the HAZ. Note that in general, the dissolution rate of precipitates in the HAZ depends on temperature (i.e., the distance from the fusion line), holding time (i.e., a function of heat input), particle size and composition, and C and N levels in the BM [15]. The Ashby–Easterling theory of particle dissolution deals with the volume fraction to be dissolved and does not take 'size' directly into consideration. This is likely one of the main limitations of the theory. For instance, TEM replica examination revealed that small NbC particles (<20 nm) were completely dissolved in the CGHAZ of a low heat-input sample (0.5 kJ/mm), where the thermal cycle was too fast for the complete dissolution of the intermediate-size NbC precipitates (50–300 nm). This could not be directly predicted by the theoretical analysis used here.

Another model for precipitate dissolution is the Whelan–Aaron–Agren invariant size/field approximation model [16] that was derived originally for dissolution under isothermal heating (i.e., heat treating as opposed to welding). In this model a simplified solution was obtained to estimate the particle size and volume fraction as a function of time by neglecting a time-dependent term that arrived from the transient part of the equation [17], i.e., a steady state solute profile was assumed. Anderson and Grong [17] suggested that the model could be used in continuous heating and cooling by numerical integration of the simplified form over the time of a thermal cycle. This idea has been favoured by several researchers (e.g., [18, 19]) since then for particle dissolution analysis in the HAZ, when the matrix contained one type of precipitate (whether simple or complex). The use of such a model for examination of particle dissolution in the Grade 100 steel (containing several types of precipitates) and comparison of the results with the results of Ashby–Easterling theory of particle dissolution presented here is beyond the scope of this article.

It was found both theoretically and experimentally that particle coarsening and reprecipitation were very limited in the fast thermal cycle of the welding experienced in this investigation, for the sizes and compositions of the precipitates present in the BM of the Grade 100 steel. Particle coarsening of Ti-rich precipitates in the CGHAZ has been reported for small particles (e.g., with mean particle size of 4 nm and a heat input of 3 kJ/mm [20] or with mean particle size of 20–40 nm and high heat inputs of

10–50 kJ/mm [21]). Precipitate dissolution was the most significant change in the HAZ of the Grade 100 steel.

Microstructural changes in the HAZ of transformable steels depend greatly on the precipitate behavior. These effects are mainly through prior austenite conditions (namely grain size and effective composition) that are affected by precipitate behavior. Precipitates can pin the austenite grain boundaries and prevent or delay austenite grain growth during the heating leg and part of the cooling leg of the thermal cycle. Even after dissolution, local enrichment of the microalloying elements is believed to have a significant solute drag effect on grain boundary movement and grain growth. Dissolution of the precipitates enriches the matrix locally with microalloying elements, as complete homogenization will not occur during the HAZ thermal cycle. Carbon enrichment may not be as localized due to the high diffusion rate of interstitial atoms at high temperatures in austenite. Such chemical composition changes, which were presented graphically in Fig. 6, can increase the hardenability (i.e., a function of carbon equivalent) as well as the hardness of the martensitic phase (i.e., a function of carbon content) [22]. It is suggested that Nb in solution can lower the transformation start temperature through a solute drag effect on decomposing austenite grain boundaries [23]. Hardenability also increases with prior austenite grains size. The effect of precipitate dissolution on microstructural changes (i.e., prior austenite grain size and final transformation products) and microhardness variation across the HAZ in the Grade 100 steel was discussed elsewhere [11].

Microstructural analysis showed the importance of optimizing the BM precipitate type and size distribution to minimize the width of the CGHAZ sub-region and the size of the prior austenite grains in this sub-region. The fracture toughness of the HAZ is affected by prior austenite grain size (PAGS) as well as the precipitate size. Ferrite laths in the bainitic and martensitic structures in the CGHAZ may have low-angle boundaries, which would not provide an obstacle to crack propagation. Therefore, the prior austenite grains that have high-angle boundaries will be the decisive factor in fracture toughness. The interfaces of large TiN particles may act as crack initiation points. Large TiN particles are not effective in grain growth control (or dispersion hardening), due to their large inter-particle spacing. Research has shown that optimizing microalloy and N content can result in the formation of small and intermediate-size TiN instead of large TiN particles (e.g., [24] or [25]), which would be more beneficial in PAGS control in the CGHAZ. It is believed that it is the fine precipitates (<50 nm) that act as grain growth controllers and contribute to the strength [26, 27]. A recommendation on composition modification (particularly reduction of Ti and Nb contents—Nb to a lesser extent) was provided to the supporting industry based on the results of this investigation [11]. Modification of the Grade 100 steel chemistry by lowering microalloy and interstitial levels resulted in finer precipitates (particularly TiN particles) and improved impact toughness [28].

Conclusions

The following conclusions can be drawn from this investigation:

(1) Large TiN and intermediate-size Ti-rich carbonitrides did not change in most regions of the HAZ. TiN may have a maximum dissolution of about 15% close to the fusion line for a heat input of 2.5 kJ/mm, based on theoretical analysis.
(2) The kinetic calculations showed that the dissolution of pure NbC can start close to the FGHAZ/CGHAZ boundary; the exact location depending on the heat input. This means that the intermediate-size Ti–Nb precipitates do not dissolve in the FGHAZ. The Nb-rich intermediate-size precipitates, however, dissolve to a large extent in the CGHAZ, especially for higher heat inputs of 1.5 and 2.5 kJ/mm.
(3) Reprecipitation is generally suppressed in the CGHAZ of the 0.5 kJ/mm weld sample. There was some reprecipitation in the CGHAZ of higher heat-input weld samples (in the form of fine precipitates) within the matrix, on the grain/lath boundaries and on the remaining intermediate-size precipitates.
(4) The size distributions of fine carbides (<20 nm) in the FGHAZ of various weld samples (0.5–2.5 kJ/mm) showed little change from the distribution in the BM, suggesting no or little dissolution in the FGHAZ.
(5) Coarsening of TiN does not occur in the HAZ of the Grade 100 steel, mainly due to the large size of these particles in the steel examined.

Acknowledgements The authors wish to thank the Natural Sciences and Engineering Research Council (NSERC) of Canada and Evraz Inc. NA for financial support and steel plates (Evraz).

References

1. DeArdo AJ (1995) Modern thermomechanical processing of microalloyed steel: a physical metallurgy perspective. Iron & Steel Society, Pittsburgh, p 15
2. Tanaka T (1995) Science and technology of hot rolling process of steel. Iron & Steel Society, Pittsburgh, p 165
3. Pereloma EV, Bayley C, Boyd JD (1996) Mater Sci Eng A 210(1–2):16
4. Gladman T (1997) The physical metallurgy of microalloyed steels. The Institute of Materials, London

5. Poorhaydari K, Ivey DG (2009) Can Metall Q 48(4):443
6. Poorhaydari K, Ivey DG (2009) Can Metall Q 48(2):115
7. DeArdo AJ (2003) Int Mater Rev 48(6):371
8. Ashby MF, Easterling KE (1982) Acta Metall 30(11):1969
9. Ion JC, Easterling KE, Ashby MF (1984) Acta Metall 32(11): 1949
10. Easterling KE (1992) Introduction to the physical metallurgy of welding. Butterworth-Heinemann Ltd, Oxford
11. Poorhaydari K (2005) Microstructure and property examination of weld HAZ in Grade 100 microalloyed steel. Ph.D. Thesis, University of Alberta, Edmonton, Canada
12. Poorhaydari K, Patchett BM, Ivey DG (2005) Estimation of cooling rate in the welding of plates with intermediate thickness. Weld J 84(10):149-s–155-s
13. Ruhle M (1995) In: ASM handbook vol 9. Metallography and microstructures. ASM International, Materials Park, OH, p 103
14. Poorhaydari K, Ivey DG (2007) Mater Charact 58(6):544
15. Suzuki S, Weatherly GC (1985) In: Gray JM, Ko T, Zhang SH, Wu BR, Xie XS (eds) Characterization of precipitates and grain growth in simulated HAZ thermal cycles of Ti–Nb bearing steel weldments. ASM International, China, p 675
16. Agren J (1990) Scand J Metall 19(1):2
17. Andersen I, Grong O (1995) Acta Metall Mater 43(7):2673
18. Shome M, Sarma DS, Gupta OP, Mohanty ON (2003) ISIJ Int 43(9):1431
19. Moon J, Jeong H, Lee J, Lee C (2008) Mater Sci Eng A 483–484:633
20. Moon J, Lee C (2009) Acta Mater 57(7):2311
21. Wang HR, Wang W (2009) J Mater Sci 44(2):591. doi:10.1007/s10853-008-3069-0
22. Fossaert C, Rees G, Maurickx T, Bhadeshia HKDH (1995) Metall Mater Trans A 26A(1):21
23. Palmiere EJ, Garcia CI, Ardo AJD (1994) Metall Mater Trans A 25(2):277
24. Liao FC, Liu S, Olson DL (1994) Effect of titanium nitride precipitates on the weldability of nitrogen enhanced Ti–V microalloyed steels. Iron and Steel Society, Inc., Pittsburgh, Pennsylvania, p 511
25. McGurk TE, Speer JG, Matlock DK (2007) Mater Sci Technol 6:347
26. Hulka K, Heisterkamp F (1998) Mater Sci Forum 284–286:343
27. Dolby RE (1983) Met Technol 10(9):349
28. Collins LE, Klein R, Bai D (2009) Can Metall Q 48(3):261